CHEMISTRY OF MATERIALS

ARTICLE

pubs.acs.org/cm

Long-Range and Short-Range Structure of Proton-Conducting Y:$BaZrO_3$

Francesco Giannici,*[,†] Mona Shirpour,[‡] Alessandro Longo,[§] Antonino Martorana,[†] Rotraut Merkle,[‡] and Joachim Maier[‡]

[†]Dipartimento di Chimica "Stanislao Cannizzaro", Università di Palermo, Italy

[‡]Max-Planck Institute for Solid State Research, Stuttgart, Germany

[§]Istituto per lo Studio dei Materiali Nanostrutturati, Consiglio Nazionale delle Ricerche, Palermo, Italy

Supporting Information

ABSTRACT: Yttrium-doped barium zirconate (BZY) is the most promising candidate for proton-conducting ceramics and has been extensively studied in recent years. The detailed features of the crystal structure, both short-range and long-range, as well as the crystal chemistry driving the doping process, are largely unknown. We use very high resolution X-ray diffraction (HR-XRD) to resolve the crystal structure, which is very slightly tetragonally distorted in BZY, while the local environment around Zr^{4+} and Y^{3+} is probed with extended X-ray absorption fine structure (EXAFS), and the symmetry and vibrations are investigated by using Raman spectroscopy. It is found that barium zirconate shows some degree of local deviation from the cubic arystotype even if undoped, which upon substitution by the perceptibly larger Y^{3+}, playing the role of a rigid inclusion, is further increased. This distortion is one limiting factor concerning the Y^{3+} solubility. The effects are correlated to the proton conduction properties of BZY.

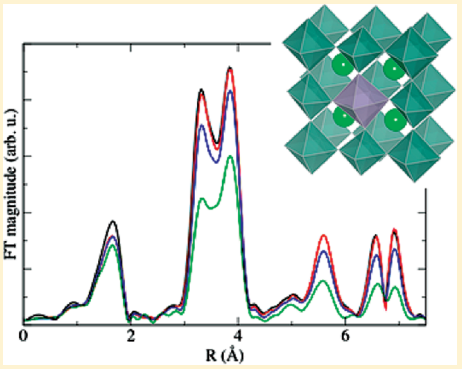

KEYWORDS: barium zirconate, proton conductor, EXAFS, XRD, Raman

1. INTRODUCTION

Since their discovery by Iwahara in the early 1980s, solid oxide proton conductors have been among the most studied materials for electrochemical applications, e.g., fuel cells, sensors, and electrochemical reactors.[1−3] The low activation energy associated with the proton transport makes them useful for mid-temperature applications (300−500 °C). In particular, acceptor-doped perovskites represent the most studied class of proton-conducting oxides, and yttrium-doped barium zirconate ($BaZr_{1-x}Y_xO_{3-y}$, BZY) has estabilizhed itself as the most promising material in the past decade. Much research effort has been devoted to achieving BZY with high stability, conductivity, and sinterability, by choosing different chemical and physical preparation methods, while the fundamental structure −property relationships have been rather overlooked in the last years. In particular, the role of the dopant on both the crystal structure and the electronic structure of the host oxide has been identified as a crucial point to be investigated.[3] Different dopants have been shown to critically influence the local structure and performance of the host materials, e.g., inducing symmetry changes, and modifiying proton concentration and mobility.[4−6]

The Goldschmidt tolerance factor, t, is a function of the ionic radii of the cations in the A- and B-sites, and it has been used to predict the lattice distortions in ABO_3 perovskites. Its value is unity when the ionic radii perfectly match in the cubic aristotype; if smaller than unity, the cation in the B-site is too large with respect to the A-site, and to accommodate it, the lattice distorts, usually by tilting the octahedra. For instance, in $BaCeO_3$, $t = 0.94$, and the unit cell is orthorhombic. In undoped barium zirconate ($BaZrO_3$, BZ), t is 1.004, indicating a very good match between Zr^{4+} and Ba^{2+}, and the unit cell is cubic. Y^{3+}, on the other hand, has a significantly larger ionic radius (0.9 Å instead of 0.72 Å) so that if incorporated in BZ, some type of distortion is expected. Of course, the tolerance factor alone is not adequate to predict the local modifications of the lattice. Rather, it is necessary to apply site-selective techniques such as X-ray absorption spectroscopy, extended X-ray absorption fine structure (EXAFS), or a technique which is sensitive to symmetry breaking, such as Raman spectroscopy. In addition to applying these techniques which probe the local structure, we performed high-resolution X-ray diffraction (HR-XRD) experiments with synchrotron radiation, thereby obtaining a complete structural characterization of Y-doped barium zirconate on both short- and long-range scales.

The subtle interplay between dopant insertion, crystal structure, and conductivity in BZY was first addressed by Kreuer and co-workers.[6] However, despite the large number of papers devoted

Received: March 7, 2011
Revised: April 26, 2011
Published: May 05, 2011

to BZY that have appeared in the past decade, the main questions concerning structure and dynamics are still a matter of debate. In particular, the finer details of the crystal structure are still unclear, the local structure around the different cations has never been elucidated, and the relationships that link the structure with the electrochemical properties are not ultimately understood. In fact, several different crystal structures have been proposed by different authors: Schober and Bohn reported BZ and BZY to be cubic up to and including 10% dopant content.[7] Kreuer et al. reported a tetragonal *P4 mm* unit cell for doping content ≥10%, while Yamazaki et al. reported cubic phases for dopant contents up to 40%.[6,8] It should be noted that these studies were all based on laboratory XRD, and therefore, the chance to detect the subtle details of the lattice distortions was determined by the instrumental resolution and accuracy of the data analysis procedure (whether indexing or full-pattern modeling).

The formation of ionic charge carriers in ion conductors typically requires doping of a host crystal structure with aliovalent atoms. In general, a good dopant should be chosen such that its presence (in electrolytes in perceptible amounts; in contrast to semiconductors) does not lead to a decrease in long-range symmetry (or rather an increase, Y-doped ZrO_2 being the most prominent example). On a short-range scale, some local distortion (e.g., due to moderately oversized dopants) may be tolerable if this helps to decrease other detrimental short-range interactions such as strong electrostatic dopant−charge carrier attraction (as suggested for Y doping in proton-conducting $BaZrO_3$ by ab initio as well as pair potential calculations).[9,10] Thus, a thorough understanding of ionic conductivity requires structural investigations on both length scales.

In this respect, we present the first application of very high-resolution XRD to a proton-conducting oxide, to resolve the crystal structure of BZ doped with Y^{3+} up to 15%. These results are correlated with two techniques probing the local features of structure and bonding, i.e., EXAFS and Raman spectroscopy, representing the first combined structural characterization of BZY. These techniques ideally complement XRD, especially in the study of doped materials. The EXAFS analysis has been successfully employed recently for the study of several trivalent dopants in proton-conducting barium cerates and zirconates.[4,5,11−14] Applications of Raman spectroscopy to several different proton conductors were first reviewed by Frech.[15] In recent years, this technique has been used by several groups, although sporadically and to varying degrees of depth, also for the investigation of barium perovskites.[16−23]

2. EXPERIMENTAL SECTION

High purity $BaCO_3$, ZrO_2 (TZ-0, Tosoh), at 6% and 15% Y-stabilized ZrO_2 (TZ-3, TZ-8, Tosoh), were used to prepare undoped and doped $BaZrO_3$. In the following, the abbreviation BZYx will be used for $BaZr_{1-x}Y_xO_{3-y}$ compounds, with "DRY" or "HYD" to indicate whether they are in the nominally dry or hydrated state, respectively. A single-phase powder was obtained after 3 steps of calcination and ball milling (Retsch VM1, equipped with a zirconia jar and balls). The stoichiometric mixture of oxides/carbonates was calcined at 1100 °C in air for 1.5 h followed by 2 h of ball milling. In the next two steps, the ground powder was calcined at 1300 °C for 3 h. The cold isostatically pressed pellets were sintered in air at 1700 °C for 20 h. For the measurements, the sintered pellets were reground to fine powders. Undoped $BaZrO_3$, abbreviated as BZ, was used as prepared. For the doped compounds, dry samples were prepared by keeping the ground pellets at 900 °C under vacuum (8×10^{-4} mbar) for 2 h, then cooling down under dry N_2 flux. Hydrated samples were prepared by heating to 900 °C and cooling down under wet N_2 (pH_2O = 20 mbar) at a very slow rate of 10 °C/h, to achieve maximum hydration. The cation concentration in the samples was measured by ICP-OES (Spectro Ciros CCD, Spectro Analytical Instruments). The powders were dissolved by high pressure microwave-assisted decomposition in HCl (37%) at 220 °C for 1.5 h. As an example, the BZY6DRY powders have the following composition: $Ba_{0.98\pm0.01}Zr_{0.94\pm0.009}Y_{0.06\pm0.002}O_{3-y}$.

High-resolution XRD was collected in transmission geometry at the ID31 beamline of the European Synchrotron Radiation Facility (ESRF, Grenoble). The incident wavelength was λ = 0.4 Å, the sample was mounted in a spinning glass capillary, and the diffracted radiation was collected by a bank of eight Si(111) analyzer crystals in front of scintillation detectors in the q-range between 0.5 and 10 $Å^{-1}$ ($q = 4\pi \sin\theta/\lambda$). The diffraction patterns were analyzed with GSAS.[24] Incident wavelength, zero displacement, and instrumental broadening were determined with Si and LaB_6 standards, and fixed during the fitting. The instrumental contribution to the fwhm was about 0.003°. During the refinement, the following parameters were refined: background, lattice parameters, atomic positions, strain broadening, and isotropic thermal parameters.

EXAFS measurements were collected at the BM29 beamline of ESRF (6 GeV, 200 mA) on the Zr K-edge (18 keV) and on the Y K-edge (17 keV). Transmission geometry was used, with the incident and transmitted intensity measured with two ionization chambers. The S_0^2 values were calibrated with BZ and Y_2O_3, and subsequently used to fit the data. Energy alignment of the spectra was carried out by placing a standard after the second ionization chamber. All measurements were taken at 25 K and analyzed using Feff8.4 and Viper.[25,26]

The Raman spectra were taken with a Jobin Yvon LabRam V010 single grating spectrometer, equipped with a double super Razor Edge filter and a Peltier cooled CCD camera. Spectra are taken in quasi-backscattering geometry using the linearly polarized 632.817 nm line of a He/Ne gas laser, with power <1 mW and filter D 0.6 focused on a 5 μm spot through a 100× microscope objective onto the top surface of the powder sample. The resolution of the spectrometer (grating 1800 L/mm) is 1 wavenumber (cm^{-1}).

3. RESULTS

3.1. X-ray Diffraction. The only previous account of the BZY crystal structure with diffraction methods other than laboratory XRD was given recently by Azad et al.: using neutron powder diffraction, they proposed that two different cubic phases are present in BZY10 (the actual amount depending on preparation and sintering conditions) and that in the one with the larger unit cell a partial substitution of Y in the Ba site takes place.[27] This model involves a significant exsolution of BaO or evaporation in order to create $Y^{\bullet}_{Ba}$ defects (positively charged Y^{3+} in the Ba^{2+} site).

The Rietveld refinements on the high-resolution XRD with synchrotron radiation data of BZ, BZY6HYD, and BZY15HYD confirm the phase purity of all samples. The results of the Rietveld refinements are reported in Table 1. For undoped BZ, a cubic *Pm-3 m* unit cell gives satisfactory results, in agreement with the literature.[28,29] On the contrary, a tetragonal cell (*P4/mbm*) is needed to fit the doped samples BZY6HYD and BZY15HYD (see Figure 1). Such a tetragonal cell can be compared with the cubic cell by the following formulas: $a_{p1} = a/(2)^{1/2} = b/(2)^{1/2}$, and $a_{p2} = c$, where a_{p1} and ap_2 are the equivalent lattice parameters. For both the doped BZY samples, the tetragonal distortion is indeed very slight ($a_{p2} - a_{p1} < 0.1\%$), nonetheless necessary to obtain a satisfactory fit. The increase of

Table 1. Results from HR-XRD Rietveld Refinements for BZ, BZY6HYD, and BZY15HYD[a]

	BZ	BZY6HYD	BZY15HYD
a (Å)	4.1931(1)	5.9438(2)	5.9716(2)
c (Å)		4.1991(1)	4.2267(1)
V_{eq} (Å^3)	73.723	74.174	75.36
U_{Ba} (Å^2)	0.005(1)	0.005(1)	0.012(2)
$U_{Zr/Y}$ (Å^2)	0.005(1)	0.005(1)	0.005(1)
U_O (Å^2)	0.009(2)	0.013(2)	0.016(2)

[a] a and c are the lattice parameters, V_{eq} is the equivalent cubic unit cell volume calculated with a_p, and U are the thermal parameters. Atomic positions in the cubic cell: Ba (1/2; 1/2; 1/2); Zr (0; 0; 0); O (1/2; 0; 0). Atomic positions in the tetragonal cell: Ba (0; 1/2; 1/2); Zr/Y (0; 0; 0); O1 (0; 0; 1/2); O2 (1/4; 3/4; 0). In the tetragonal cell, oxygen atoms have the same thermal parameter, U_O.

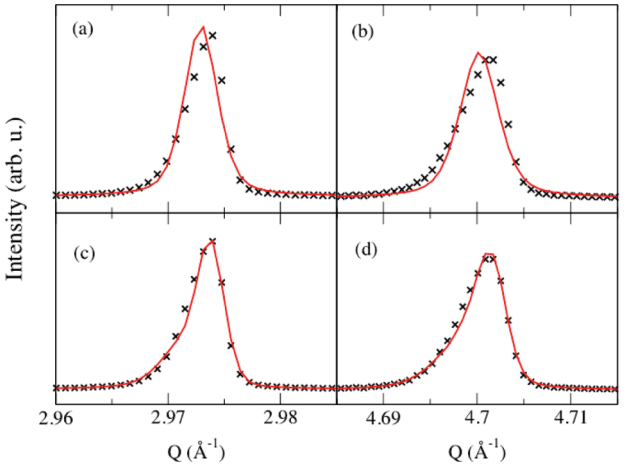

Figure 1. Comparison of the XRD best fitting for BZY15HYD, obtained with cubic (panels a and b) or tetragonal (panels c and d) models. The two peaks correspond to the (200) and (310) reflections of the cubic unit cell, respectively.

the unit cell volume with dopant content is in agreement with the results by Kreuer et al.[6]

In BZ, the Bragg peaks are broadened by both instrumental and particle size effects, which dominate, respectively, at low and high angles. On the contrary, the peak broadening in Y-doped samples is largely dominated by strain in the whole Q-range so that the broadening increases steeply with the scattering angle. For this reason, two parameters were refined to take into account the anisotropic strain broadening, which accounts for the significant peak asymmetry at higher angles. The large broadening of the peaks can also be appreciated visually from the comparison of the diffraction patterns of undoped BZ and BZY6HYD in Figures 2 and 3. The thermal parameters for Ba^{2+} and O^{2-} increase with Y^{3+} content, while the thermal parameter for the B-site is constant. This suggests that the dopant is not displaced from its lattice site upon insertion, while inducing significant perturbation in its local environment.

It is worth noting that the thermal parameter for the O^{2-} site is significantly larger than the other ones also in undoped BZ, where it is 0.009 Å^2. For comparison, in undoped $SrTiO_3$ (which is also a cubic perovskite) the U_O parameter is 0.006 Å^2, which is also of the same order of magnitude as U_{Sr} and U_{Ti}.[30] We also

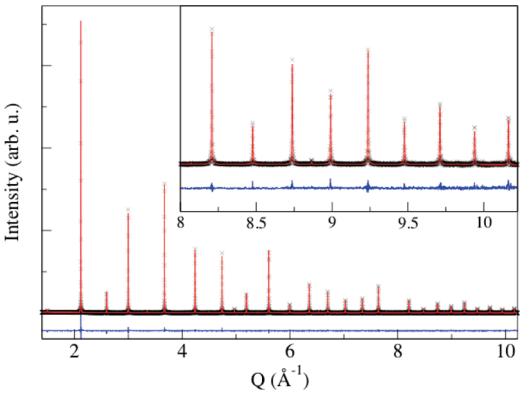

Figure 2. XRD data and model for undoped BZ.

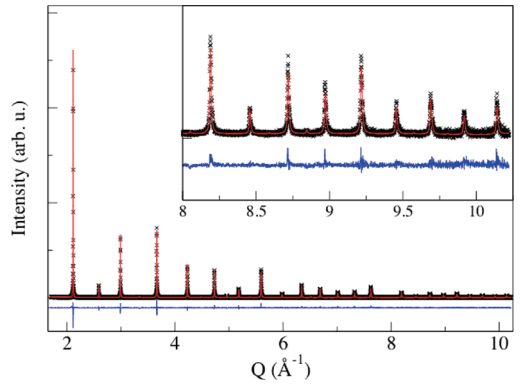

Figure 3. XRD data and model for BZY6HYD.

considered the two-phase model proposed by Azad et al., composed of two cubic phases with a = 4.205 and a = 4.193 Å.[27] In fact, such a splitting (Δa = 0.3%) between the Bragg peaks is not compatible with the present experimental data, suggesting that the two phases are found only in samples prepared at lower temperatures.

3.2. EXAFS: Zr K- and Y K-Edges. More details about the effects of the Y^{3+} dopant on the structure can be obtained from EXAFS at the Zr and Y K-edges. The structural model used to fit the data on the Zr K-edge is constructed as follows: (a) Zr−O first shell; (b) Zr−Ba second shell; (c) Zr−M third shell (M = Zr,Y), including Zr−O−M multiple scattering paths; (d) Zr−O2 fourth shell; (e) Zr−M2 fifth shell. Each shell has independent distances and disorder factors. The coordination numbers of the cations are fixed, while the first shell coordination number was refined to account for the oxygen deficiency, and the coordination number of the fourth shell was constrained accordingly. The number of independent points according to the Nyquist criterion is about 60, with 15 fitting parameters. The model around Y^{3+} does not include the fifth shell; therefore, there are about 35 independent points and 13 fitting parameters: even in this latter case, there are more than twice the independent points as free parameters, assuring very robust fitting and reliable results. The quality of the fitting in both k-space and R-space can be appreciated in Figures 4 to 7, and the Fourier-transformed data for the different samples are plotted together in Figures 8 (Zr K-edge) and 9 (Y K-edge). All of the fitting results are collected in Tables 2 and 3. Uncertainty on the results of the EXAFS analysis is about 0.5 for coordination numbers, 0.02 Å for distances, and 10^{-4} Å^2 for disorder factors.

dx.doi.org/10.1021/cm200682d |*Chem. Mater.* 2011, 23, 2994–3002

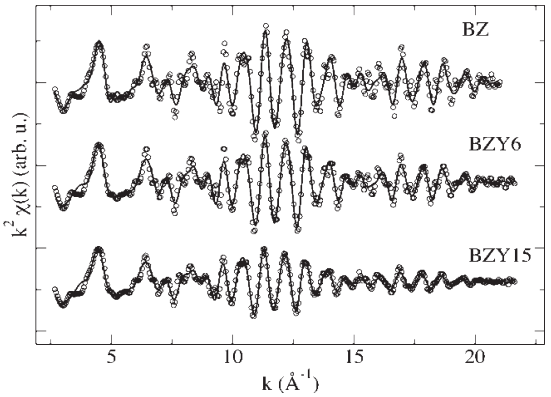

Figure 4. Zr K-edge EXAFS data (circles) and best fit (thick line) of hydrated BZY samples.

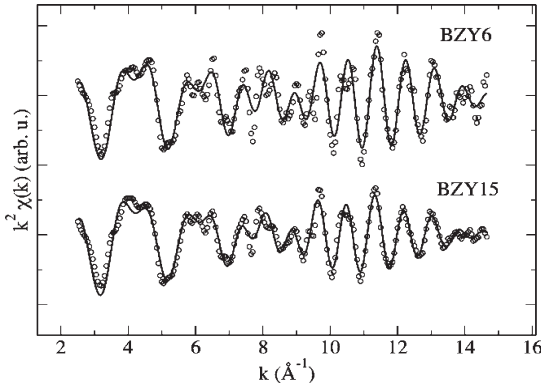

Figure 5. Y K-edge EXAFS data (circles) and best fit (thick line) of hydrated BZY samples.

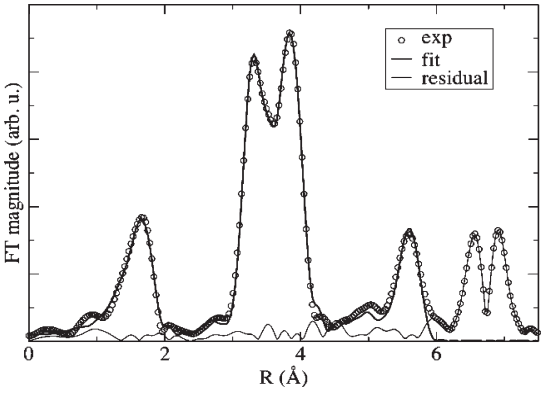

Figure 6. Fourier-transformed Zr K-edge EXAFS data (circles), best fit (thick line), and residual (thin line) of undoped BZ.

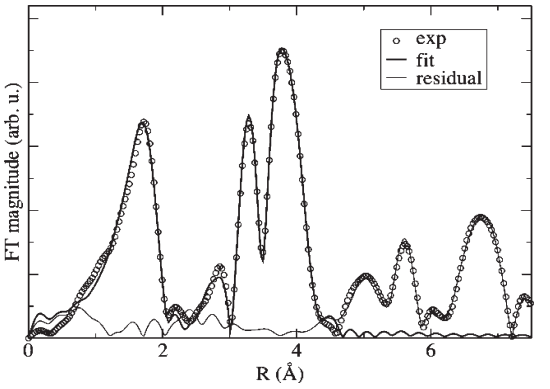

Figure 7. Fourier-transformed Y K-edge EXAFS data (circles), best fit (thick line), and residual (thin line) of BZY6HYD.

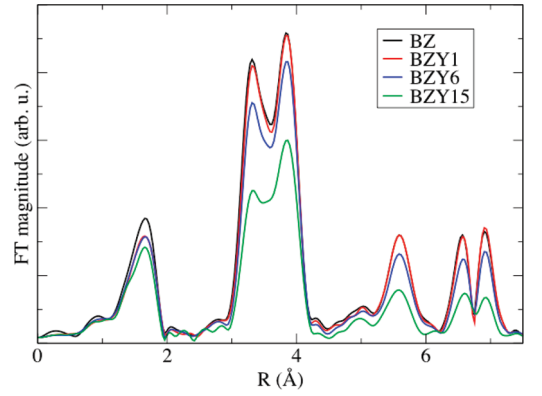

Figure 8. Comparison of Fourier-transformed Zr K-edge EXAFS data of hydrated BZY samples.

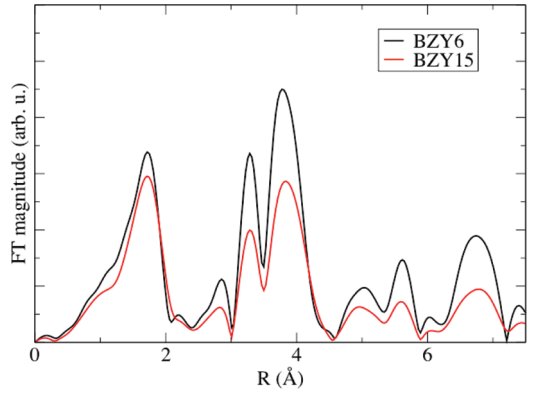

Figure 9. Comparison of Fourier-transformed Y K-edge EXAFS data of hydrated BZY samples.

As already suggested by the XRD analysis, there is no sign of dopant segregation. Moreover, there are no hints of a possible substitution of Y^{3+} in the site of Ba^{2+}. The data analysis on the Y K-edge provides evidence of an effective Y^{3+} inclusion in the B-site of the perovskite structure. In particular, there are no spurious peaks around 3 Å that could be attributed to the Y−Y correlations in Y_2O_3, and the model satisfactorily reproduces all of the observed features up to 4.5 Å.[9] Moreover, no hints of $Y^{\bullet}_{Ba}$ defects can be detected, despite the very slight Ba deficiency evidenced in the chemical analysis. In all samples, the fitted coordination numbers for the Zr−O and Y−O first shell did not deviate from the stoichiometric value (6) within the sensitivity of the technique (around 0.5). BZY6DRY showed a reduction of the Y−O first shell coordination number to 5.6, hinting at a possible $Y-V_O^{\bullet\bullet}$ association: however, such an effect is not confirmed by the BZY15DRY sample.

In Figures 10 to 13, all of the interatomic distances around Zr and Y are plotted as a function of the dopant content, along with

dx.doi.org/10.1021/cm200682d |*Chem. Mater.* 2011, 23, 2994–3002

Table 2. EXAFS Results for Dry and Hydrated BZY on the Y K-Edge[a]

		BZY6HYD	BZY6DRY	BZY15HYD	BZY15DRY
Y-O	N	6.0	5.6	6.0	6.0
	R	2.21	2.21	2.23	2.22
	σ^2	6.4	5.6	6.2	7.4
Y-Ba	R	3.64	3.64	3.65	3.65
	σ^2	5.6	5.7	7.0	7.4
Y-M	R	4.21	4.21	4.24	4.23
	σ^2	4.6	5.0	5.8	5.9
Y-O2	R	4.74	4.73	4.77	4.77
	σ^2	11	14	14	13

[a] Distances are in Å and disorder factors in 10^{-3} Å^2.

Table 3. EXAFS Results for Dry and Hydrated BZY on the Zr K-Edge[a]

		BZ	BZY1 HYD	BZY6 HYD	BZY6 DRY	BZY15 HYD	BZY15 DRY
Zr−O	N	6.0	6.0	6.0	5.9	6.0	5.9
	R	2.10	2.11	2.11	2.11	2.11	2.11
	σ^2	3.2	4.2	4.2	4.0	5.5	5.0
Zr−Ba	R	3.63	3.64	3.64	3.64	3.65	3.65
	σ^2	2.4	2.5	2.9	2.9	4.4	4.1
Zr−M	R	4.20	4.20	4.21	4.22	4.22	4.22
	σ^2	1.4	2.3	2.6	2.8	3.7	3.6
Zr−O2	R	4.67	4.67	4.67	4.66	4.69	4.68
	σ^2	3.8	5.1	5.6	5.5	8.2	7.5
Zr−M2	R	5.90	5.95	5.96	5.96	5.98	5.97
	σ^2	2.7	2.2	2.8	2.7	4.7	4.2

[a] Distances are in Å and disorder factors in 10^{-3} Å^2.

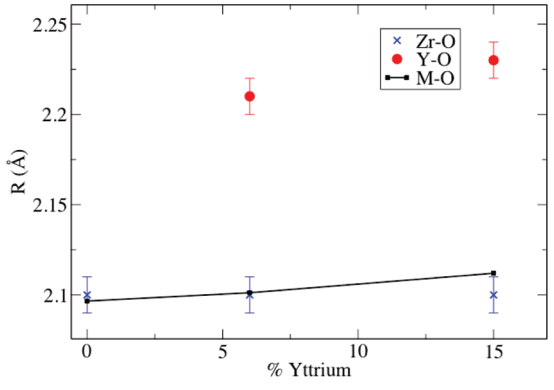

Figure 10. Comparison of first shell Zr−O, Y−O, and M−O distances probed by XRD and EXAFS as a function of Y^{3+} content in hydrated BZY samples.

the corresponding distances around the perovskites B-sites calculated from X-ray diffraction. The Y−O1 distance is always found to be greater than Zr−O1, both very slightly increasing with increasing dopant content, and the experimental difference (0.1−0.12 Å) is lower than what can be expected from the simple comparison of the ionic radii (0.18 Å).[31] These findings are also valid for the fourth shell Zr−O2 and Y−O2 distances: Y−O2 is always significantly larger than Zr−O2, and they increase slightly with the dopant concentration.

In conclusion, the anion sublattice expands significantly around the trivalent dopants, the magnitude of such expansion decreasing as expected as one moves farther from the doped sites. Diffraction techniques detect a single distance, which results from

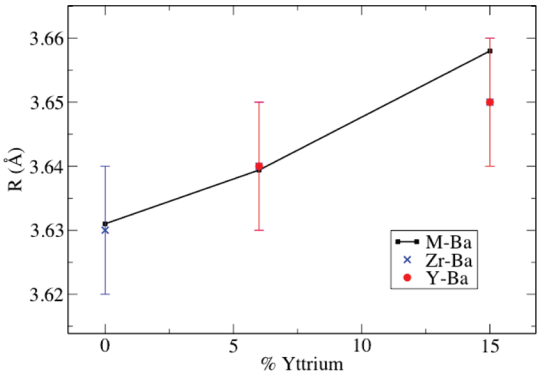

Figure 11. Comparison of second shell Zr−Ba, Y−Ba, and M−Ba distances probed by XRD and EXAFS as a function of Y^{3+} content in hydrated BZY samples. Note that for BZY6 and BZY15, the Zr−Ba symbols and error bars are covered by Y−Ba.

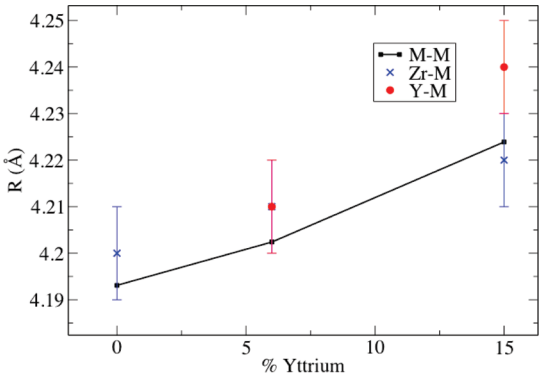

Figure 12. Comparison of third shell Zr−M, Y−M, and M−M distances probed by XRD and EXAFS as a function of Y^{3+} content in hydrated BZY samples. Note that for BZY6, the Zr−M symbol and error bars are covered by Y−M.

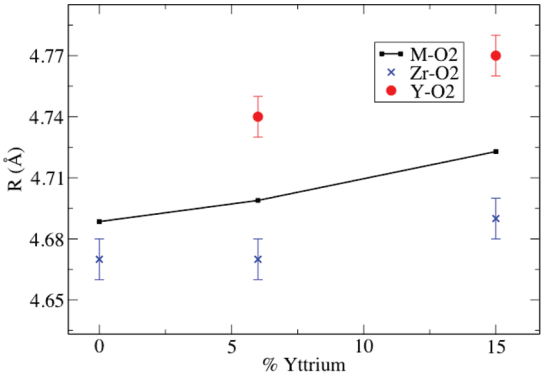

Figure 13. Comparison of fourth shell Zr−O, Y−O, and M−O distances probed by XRD and EXAFS as a function of Y^{3+} content in hydrated BZY samples.

the averaging over undoped and doped sites. The cation sublattice responds quite differently to the dopant insertion. In fact, Y−Ba and Zr−Ba fitted values are equal in both BZY6 and BZY15. The third shell distances Zr−M and Y−M are also equal in BZY6, and very similar in BZY15: the increase of these interatomic distances as a function of the dopant content very closely reflects the average increase seen with HR-XRD. Moreover, it can be argued that since the distance between the perovskite B-sites is maintained around the Y^{3+} dopant, while the YO_6 octahedron is remarkably larger than ZrO_6, the YO_6 unit is tilted with respect to the neighboring octahedra, in order to fit into the lattice. This hypothesis receives further confirmation from the Raman results reported below.

The EXAFS disorder factors, σ^2, represent the spreading of the interatomic distances around each site: this includes both static disorder (many different equilibrium distances) and dynamic disorder (stretching of the interatomic distance). From an inspection of the values reported in Tables 2 and 3, it can be seen that every interatomic distance around Y^{3+} has a much higher disorder than the corresponding distance around Zr^{4+}. This is true for both hydrated and dry samples. A significant increase in the disorder factors of the second and farther shells around Zr^{4+} with increasing dopant content is evident from the damping of the peaks above 3 Å in Figures 8 and 9. The Zr−O first shell disorder is also somewhat increased with higher dopant content, although in this case the effect is less marked. The local environment of Y^{3+} is also affected by higher disorder when the dopant content is increased from 6% to 15%: in particular, the Y−O disorder is almost unaffected, while the Y−Ba and Y−M disorder factors increase much more strongly. Interestingly, the Y−O2 disorder is very large (>0.01 $Å^2$) despite the fact that σ^2(Y−M) is only moderately larger than σ^2(Zr−M): as the strain due to the size mismatch between Y^{3+} and Zr^{4+} is released preferentially through the expansion of the anion sublattice, the disorder also concentrates on oxygen atoms after the insertion of the dopant. In dry samples, the disorder around Zr^{4+} is slightly but consistently lower than that in the corresponding hydrated samples. The effect of hydration on the disorder around Y^{3+} is generally lower and not systematic, suggesting that there is no preferential interaction between the doped site and the protonic defects.

3.3. Raman Spectroscopy. According to the XRD results discussed above, undoped BZ adopts a cubic structure. In fact, its Raman spectrum shows first-order peaks that can appear only in a noncubic symmetry. Such peaks were already reported by several authors.[16−22] The Raman spectrum of cubic $SrTiO_3$, which shows only extremely broad features known to be second-order transitions,[32] is plotted together with BZ and BZY samples in Figure 14: from comparison, it is evident that the peaks in the BZ spectra are first-order transitions indicating an actual deviation from the cubic symmetry. The peaks present in the Raman spectrum of BZ are also present in the spectra of BZY samples. These can be qualitatively divided into three groups:

(i) very broad peaks around 250 cm^{-1}, 470 cm^{-1}, and 730 cm^{-1}, whose positions shift with Y^{3+} content; while the relative intensity of the 250 cm^{-1} peak increases with Y^{3+} content, the area of the peaks at 470 cm^{-1} and 730 cm^{-1} is approximately constant;

(ii) peaks around 88 cm^{-1}, and 138 cm^{-1}, whose positions are roughly independent of Y^{3+} content, while their relative intensities increase with Y^{3+} content;

(iii) peaks around 185 cm^{-1}, 350 cm^{-1}, 580 cm^{-1}, 640 cm^{-1}, and 840 cm^{-1}, whose positions are roughly independent of Y^{3+} content, and whose relative intensities decrease with Y^{3+} content;

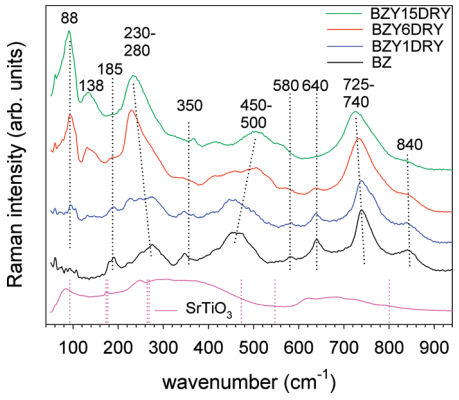

Figure 14. Raman spectra of dry BZY samples with different Y-content, along with the spectrum of undoped $SrTiO_3$. Pink dashed lines: phonon modes for cubic $SrTiO_3$.

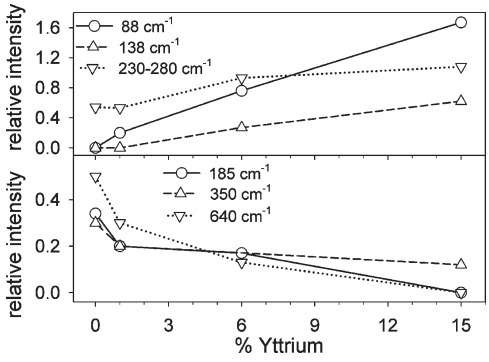

Figure 15. Relative intensity of various Raman peaks relative to the peak at 740 cm^{-1}, as a function of dopant content.

The variations of the intensity of the above peaks as a function of the dopant concentration are reported in Figure 15.

The assignment of the Raman peaks listed above is not unambiguous. A tentative assignment can be carried out by comparison with similar perovskites, such as cubic $SrTiO_3$. The hyper-Raman active modes of $SrTiO_3$ are listed in Table 4.[35] The mode TO4 corresponds to B−O stretching, TO3 to O−B−O bending, TO2 to a movement of A versus BO_6, and TO1 predominantly to a movement of O_6 versus A and B cations. $BaZrO_3$ TO modes from IR spectra are also reported for comparison. Unfortunately, frequencies from DFT calculations vary by up to 20% when different functionals or core−electron pseudopotentials are used as shown for $BaZrO_3$ and $BaTiO_3$.[34,36] The phonon frequencies of BZ and BZY are comparable to the corresponding $SrTiO_3$ modes.

The Raman spectra for undoped BZ and BZY share some common features. In fact, the appearance of several additional peaks in BZY spectra, as well as the different peak widths and intensities, all indicate that the distortion already present in undoped BZ is inherently different from the additional distortion introduced by the doping process. The peaks at 580−840 cm^{-1} can be assigned to various M−O stretching motions. The smaller peaks at 580, 640, and 840 cm^{-1} exist already for BZ and thus are due to local distortions of the anion sublattice discussed above. The peak at 740 cm^{-1} is very sensitive to the dopant concentration,

dx.doi.org/10.1021/cm200682d |Chem. Mater. 2011, 23, 2994–3002

Table 4. Assignment of $BaZrO_3$ TO Frequencies from IR Spectra and DFT Calculations, Compared with the $SrTiO_3$ Peak Assignment[a]

phonon	symmetry	$BaZrO_3$ IR (cm^{-1})	$BaZrO_3$ DFT (cm^{-1})	$SrTiO_3$ hyper-Raman (cm^{-1})
TO1	F_{1u}	115	129	88
LO1			146	175
TO2	F_{1u}	210	218	175
LO2			397	266
TO3	F_{2u}		228	266
LO3				474
TO4	F_{1u}	505	509	545
LO4			677	795

[a] TO = transverse optical; LO = longitudinal optical. $BaZrO_3$ IR assignment from ref. 33, DFT frequencies and assignment from ref. 34, $SrTiO_3$ assignment from ref. 35.

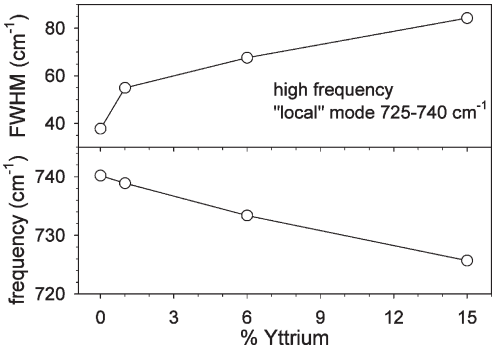

Figure 16. Variation of the position and width of the Raman peak at 740 cm^{-1} as a function of dopant content.

and it shows an approximately linear shift to lower frequencies as shown in Figure 16. The (Zr,Y)−O stretching is allowed in IR even if the local environment is cubic, while it is forbidden by symmetry in Raman. Now, the Raman peak shifts significantly on increasing the contributions from the YO_6 octahedra, while the IR peak (shown in Supporting Informations) is almost unperturbed. Then, it can be concluded that the Raman peak is essentially due to the Y−O−M tilted configurations which lower the local symmetry enough for the transition to be allowed. The Raman peak then shifts to lower wavelengths since the Y−O force constant is lower than Zr−O, as can be expected from the lower formal charge.[37] The broadening of this peak with increasing dopant content (shown in Figure 16) arises from the mixing of the different M−O contributions and is also in line with this interpretation.

The intensity of the low frequency peaks at 88, 138, and 230−280 cm^{-1} increase significantly with increasing dopant content, and the 230−280 cm^{-1} peak also shifts position. While it is present already for the undoped BZ, its broadening and shifting for BZY6 and BZY15, analogous in the case of the 725−740 cm^{-1} peak, indicates that it can be regarded as a vibration involving Y^{3+} (e.g., Ba vs YO_6 motion, as in TO2/LO2). The appearance of the peaks at 88 and 138 cm^{-1} for BZY6 and BZY15 may either be related to local symmetry reduction due to Y^{3+} substitution or to the presence of the tetragonal phase. Raman spectra of hydrated samples show little changes when compared to dry samples (see Figure 17). Previous studies

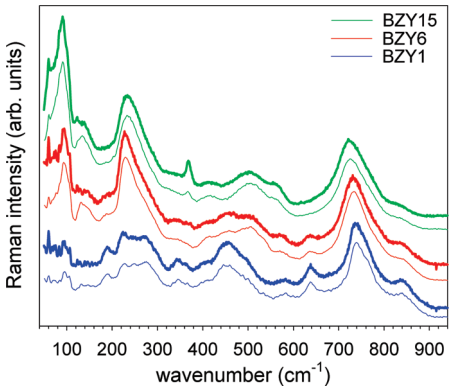

Figure 17. Raman spectra of hydrated (thick lines) and dry (thin lines) BZY samples.

on acceptor-doped $BaZrO_3$ reported very similar features for hydrated and dry samples, with the relative peak intensities sometimes differing but without systematic changes.[18,23] The peaks in the BZY-hydrated samples are a bit sharper, which might be due to the fact that singly charged OH groups on anion sites represent a smaller disturbance than doubly charged oxygen vacancies. The only significant difference is a decrease of the 138 cm^{-1} peak intensity in hydrated BZY6 and BZY15.

4. DISCUSSION

The HR-XRD data analysis shows that undoped BZ is cubic, while BZY6 and BZY15 have a tetragonal unit cell, whose deviation from the cubic symmetry is so slight that it cannot be probed with a laboratory diffractometer. The tetragonal structures reported in previous studies were most likely due to inhomogeneous compositions, owing to a spatial distribution of the dopant atoms, resulting in the splitting of diffraction peaks. However, a two-phase model as put forward by Azad et al. is not suited to fit our data, confirming the phase purity of the BZY6 and BZY15 powders under consideration. The tetragonal *P4/mbm* space group used to fit the HR-XRD data of BZY allows for a coherent tilt in one direction (tilt system: $a^0a^0c^+$).[38] In fact, such a tilting is not observed in the refined structural models since the average position of the oxygen atoms is not displaced from the crystallographic site (even if they show increased thermal parameters). Therefore, the tetragonal distortion is visible only as an elongation of the unit cell along the *c* axis. It can be argued that the model derived from diffraction is not satisfactory to describe a system with randomly distributed YO_6 octahedra that disrupt the zero-tilting pattern and whose effect is localized to a small volume around the Y^{3+} dopant cation. This is further confirmed by the increasing strain broadening that needs to be included in the Rietveld refinement of BZY6 and BZY15. Overall, thermal parameters and unit cell volume increase with doping level, also as a result of the substitution of larger Y^{3+} for Zr^{4+}.

The EXAFS analysis gives more detailed insight into the local distortions caused by Y doping. The larger size of Y^{3+} compared to Zr^{4+} results in an increased Y−O bond length, while Y−Ba and Y−(Zr/Y) have essentially the same distance as Zr−Ba and Zr−(Zr/Y). These distortions can most reasonably be described by a nonlinear Y−O−Zr arrangement (angle at O ≈ 160°), corresponding to a tilt of the YO_6 octahedra. To a certain degree, this octahedral tilt also continues for the neighboring $(Zr/Y)O_6$ octahedra, which leads to an increased Y−O2 distance and a

remarkably high Y−O2 disorder parameter. In conclusion, the strain around the larger Y^{3+} cation is released by the displacement of the anion sublattice, while the cations surrounding the dopant remain substantially unperturbed. Even in this case, as was observed in Y:$BaCeO_3$, the Y^{3+} dopant quite rigidly maintains its ionic size, acting as a rigid inclusion, without substantial adaptations to the structural features of its host lattice.[4] The association between Y^{3+} and oxygen vacancies in dry BZY samples, predicted by DFT calculations,[39] is only detected by the decrease of the first shell coordination number in BZY6, while this is not the case for BZY15. The variation of first shell disorder factors around Y^{3+} is also not systematic. In any case, the presence of vacancies associated with dopant sites is not sufficient to create enough asymmetry breaking and give rise to first-order Raman peaks.[40]

The presence of such Raman peaks indicates the presence of local symmetry reduction for BZY and even undoped BZ. While on a long-range scale undoped BZ is undoubtely a cubic perovskite, the presence of Raman peaks indicates that some local distortions also occur. This is supported by the thermal parameter for oxygen atoms, U_O, which is larger than expected for a cubic perovskite, suggesting that incoherent disorder of the anion sublattice is present. Two DFT studies predicted that undoped BZ may develop a distorted structure which is very close in energy to the cubic structure.[29,41] Because of the low energy gain by the distortion, it is likely that the effect is not strong enough for a coherent deformation, but such fluctuations can occur on a short-to medium range scale due to the related gain in configurational entropy. In the Raman spectra of BZY samples, some other features appear with increasing dopant concentration, e.g., the peaks at 88 cm^{-1}, 138 cm^{-1}, and 230−280 cm^{-1}. On the basis of the HR-XRD data, cation displacement can be ruled out as being the reason, and EXAFS shows single Y−O and Zr−O distances for the first coordination shells. A previous study on Fe:$SrTiO_3$ showed that the mere presence of oxygen vacancies and an aliovalent dopant at the B site in the perovskite do not lead to additional peaks.[40] For this reason, we propose that the Raman peaks in Y-doped BZ are due to the tilting of the YO_6 octahedra, which represent a permanent local symmetry lowering, as opposed to the transient or incoherent symmetry lowering due to anion sublattice motion in undoped BZ. The tilted Y−O−M configurations were predicted by DFT calculations for 12.5% Y-doped BZ.[42]

As far as proton conductivity is concerned, the slight local octahedral tilt introduced by the dopant (comparable to the long-range coherent tilt present in the Y:$BaCeO_3$, also having a high proton conductivity), is not expected to be detrimental since the limiting step for proton transfer in BZY is generally thought to be the intraoctahedral proton transfer.[3] The fact that the lattice distortion does not significantly increase upon water incoporation (even the Raman peak at 138 cm^{-1} decreases) is beneficial for proton conductivity since in general, a higher symmetry is believed to favor high proton mobility.[3] The above observations only hold for slight tilting of the octahedra: for instance, in $SrCeO_3$ the Ce−O−Ce angles are about 140° so that there are two chemically inequivalent oxygen sites, with negative consequences on proton mobility, and two-stage hydration behavior.[6]

The EXAFS results also show that there is at least not a very pronounced association of oxygen vacancies with the Y dopants in their first coordination sphere. Taking this as experimental indication for the absence of strong electrostatic dopant−defect attraction in Y:$BaZrO_3$, this suggests that the trapping of protons close to Y dopants is also weak.

5. CONCLUSIONS

We have investigated the local and long-range structure of BZY, with Y^{3+} content up to 16%, using synchrotron radiation techniques (HR-XRD and EXAFS) and Raman spectroscopy. The XRD data of all samples can be modeled using a single perovskite structure. Undoped BZ is cubic, while for 6% and 15% doping levels a very slight tetragonal distortion arises, along with significant microstrain. The thermal parameters of undoped BZ indicate that the anion sublattice is more disordered than expected for a cubic perovskite, and this is attributed to incoherent and/or transient local deviations from the cubic symmetry. Such deviations also account for the presence of Raman peaks which would otherwise be forbidden in cubic symmetry. The insertion of YO_6 units gives rise to a further increase of the Raman spectrum, due to the progressive reduction of local symmetry caused by the dopant inclusion. As evidenced by EXAFS, Y^{3+} is exclusively incorporated into the perovskite B-site, with a maximum load of 16%. The YO_6 octahedra are regular, and they are larger than the ZrO_6 octahedra. In this respect, Y^{3+} acts as a rigid inclusion in the host lattice. The local structure beyond the first shell is also expanded around the dopant, as a result of the size mismatch between the dopant and the host cation. However, only the anion sublattice is substantially enlarged and disordered around Y^{3+}, while the Y−M distances are equal to the Zr−M distances; to maintain the rigidity of the cation network, the Y−O−M configurations are tilted so as to provide sufficient space for the larger YO_6 units. From this combined information, it can be argued that the local distortions introduced by Y^{3+} and its inability to adapt to the symmetry of the host lattice are the main reasons behind the limited solubility of Y^{3+} in barium zirconate. It is also likely that this is some inherent feature of Y^{3+}, as it shows the same behavior when inserted in barium cerate.[9] However, the magnitude of the distortions introduced by the dopant is not enough to reduce the symmetry of the possible transfer paths during proton conduction or to cause two chemically inequivalent oxygen atoms to appear. The presence of inherent dynamical disorder in the anion sublattice of undoped barium zirconate is an unexpected and interesting feature, which could possibly be observed also in other cubic perovskites.

■ ASSOCIATED CONTENT

Ⓢ Supporting Information. IR spectra of undoped BZ and dry BZY samples (PDF). This material is available free of charge via the Internet at http://pubs.acs.org.

■ AUTHOR INFORMATION

Corresponding Author
*E-mail: giannici@pa.ismn.cnr.it.

■ ACKNOWLEDGMENT

We acknowledge the ESRF for the provision of beamtime (proposal CH-2588). We thank Dr. C. Prestipino and Dr. A. Fitch (ESRF) for assistance with the EXAFS and XRD measurements, A. Schulz (MPI for Solid State Research, Stuttgart) for asisstance with the Raman measurements, and A. Meyer (MPI for Metals Research,

Stuttgart) for the ICP-OES analysis. Financial support from MIUR under PRIN 2008 "PC-SOFCs, Protonic Conductors Solid Oxide Fuel Cells based on nanostructured proton conductors: from materials synthesis to prototype fabrication" is acknowledged.

REFERENCES

(1) Iwahara, H.; Yajima, T.; Hibino, T.; Ozaki, K.; Suzuki, H. *Solid State Ionics* **1993**, *61*, 65.
(2) Norby, T. *Solid State Ionics* **1999**, *125*, 1.
(3) Kreuer, K.-D. *Annu. Rev. Mater. Res.* **2003**, *33*, 333.
(4) Longo, A.; Giannici, F.; Balerna, A.; Ingrao, C; Deganello, F; Martorana, A *Chem. Mater.* **2006**, *18*, 5782.
(5) Giannici, F.; Longo, A.; Balerna, A.; Kreuer, K.-D.; Martorana, A. *Chem. Mater.* **2007**, *19*, 5714.
(6) Kreuer, K.-D.; Adams, S.; Munch, W.; Fuchs, A.; Klock, U.; Maier, J. *Solid State Ionics* **2001**, *145*, 295.
(7) Schober, T.; Bohn, H. G. *Solid State Ionics* **2000**, *127*, 351.
(8) Yamazaki, Y.; Babilo, P.; Haile, S. M. *Chem. Mater.* **2008**, *20*, 6352.
(9) Björketun, M. E.; Sundell, P. G.; Wahnström, G. *Phys. Rev. B* **2007**, 054307.
(10) Stokes, S. J.; Islam, M. S. *J. Mater. Chem.* **2010**, *20*, 6258.
(11) Giannici, F.; Longo, A.; Deganello, F.; Balerna, A.; Arico', A.; Martorana, A. *Solid State Ionics* **2007**, *178*, 587.
(12) Giannici, F.; Longo, A.; Balerna, A.; Kreuer, K.-D.; Martorana, A. *Chem. Mater.* **2009**, *21*, 2641.
(13) Giannici, F.; Longo, A.; Balerna, A.; Martorana, A. *Chem. Mater.* **2009**, *21*, 597.
(14) Giannici, F.; Longo, A.; Kreuer, K.-D.; Balerna, A.; Martorana, A. *Solid State Ionics* **2010**, *181*, 122.
(15) Frech, R. . In *Proton Conductors*; Colomban, P., Ed.; Cambridge University Press: Cambridge, UK, 1992; pp 377−388.
(16) Karan, N. K.; Katiyar, R. S.; Maiti, T.; Guo, R.; Bhalla, A. S. *J. Raman Spectrosc.* **2009**, *40*, 370.
(17) Dobal, P. S.; Dixit, A.; Katiyar, R. S.; Yu, Z.; Guo, R.; Bhalla, A. S. *J. Appl. Phys.* **2001**, *89*, 8085.
(18) Karlsson, M.; Matic, A.; Knee, C. S.; Ahmed, I.; Eriksson, S. G.; Borjesson, L. *Chem. Mater.* **2008**, *20*, 3480.
(19) Slodczyk, A.; Colomban, P.; Lamago, D.; Limage, M. H.; Romain, F.; Willemin, S.; Sala, B. *Ionics* **2008**, *14*, 215.
(20) Charrier-Cougoulic, I.; Pagnier, T.; Lucazeau, G. *J. Solid State Chem.* **1999**, *142*, 220.
(21) Chemarin, C.; Rosman, N.; Pagnier, T.; Lucazeau, G. *J. Solid State Chem.* **2000**, *149*, 298.
(22) Karlsson, M.; Ahmed, I.; Matic, A.; Eriksson, S. G. *Solid State Ionics* **2010**, *181*, 126.
(23) Karlsson, M.; Ahmed, I.; Matic, A.; Eriksson, S. *Solid State Ionics* **2009**, *181*, 126.
(24) Larson, A.; Von Dreele, R. B. *Rep. LAUR* **1988**, 86.
(25) Ankudinov, A. L.; Ravel, B.; Rehr, J. J.; Conradson, S. D. *Phys. Rev. B* **1998**, *58*, 7565.
(26) Klementev, K. D. *J. Phys. D: Appl. Phys.* **2001**, *34*, 209.
(27) Azad, A. K.; Savaniu, C.; Tao, S. W.; Duval, S.; Holtappels, P.; Ibberson, R. M.; Irvine, J. T. S. *J. Mater. Chem.* **2008**, *18*, 3414.
(28) Wood, E. A. *Acta Crystallogr.* **1951**, *4*, 353.
(29) Akbarzadeh, A. R.; Kornev, I.; Malibert, C.; Bellaiche, L.; Kiat, J. M. *Phys. Rev. B* **2005**, *72*, 205104.
(30) Maslen, E. N.; Spadaccini, N.; Ito, T.; Marumo, F.; Satow, Y. *Acta Crystallogr., Sect. B* **1995**, *51*, 939.
(31) Shannon, R. D. *Acta Crystallogr., Sect. A* **1976**, *32*, 751.
(32) Perry, C. H.; Fertel, J. H.; McNelly, T. F. *J. Chem. Phys.* **1967**, *47*, 1619.
(33) Perry, C. H.; McCarthy, D. J. *Phys. Rev. A* **1965**, *138*, A1537.
(34) Evarestov, R. A. *Phys. Rev. B* **2011**, *83*, 014105.
(35) Vogt, H.; Neumann, G. *Phys. Status Solidi B* **1979**, *92*, 57.
(36) Bilic, A.; Gale, J. D. *Phys. Rev. B* **2009**, *79*, 174107.
(37) Minervini, L.; Grimes, R. W.; Sickafus, K. E. *J. Am. Ceram. Soc.* **2000**, *83*, 1873.
(38) Glazer, A. M. *Acta Crystallogr., Sect. A* **1975**, *31*, 756.
(39) Sundell, P. G.; Bjorketun, M. E.; Wahnstrom, G. *Phys. Rev. B* **2006**, *73*, 104112.
(40) Vracar, M.; Kuzmin, A.; Merkle, R.; Purans, J.; Kotomin, E. A.; Maier, J.; Mathon, O. *Phys. Rev. B* **2007**, *76*, 174107.
(41) Bennett, J. W.; Grinberg, I.; Rappe, A. M. *Phys. Rev. B* **2006**, *73*, 180102.
(42) Gomez, M. A.; Chunduru, M.; Chigweshe, L.; Foster, L.; Fensin, S. J.; Fletcher, K. M.; Fernandez, L. E. *J. Chem. Phys.* **2010**, *132*, 214709.